Location of Artinite (Mg$_2$CO$_3$(OH)$_2$·3H$_2$O) within the MgO-CO$_2$-H$_2$O System using Ab initio Thermodynamics

J. S. Tse,[†] J. Grant,[‡] J. M. Skelton,[¶] L. J. Gillie,[†] R. Zhu,[§] G. L. Pesce,[‖] R. J. Ball,[⊥] S. C. Parker,[*,‡] and M. Molinari[*,†]

[†]Department of Chemistry, University of Huddersfield, Queensgate, Huddersfield, HD1 3DH, UK

[‡]Department of Chemistry, University of Bath, Claverton Down, Bath, BA2 7AY, UK

[¶]Department of Chemistry, University of Manchester, Oxford Road, Manchester M13 9PL, UK

[§]CAS Key Laboratory of Mineralogy and Metallogeny, and Guangdong Provincial Key Laboratory of Mineral Physics and Materials, Guangzhou Institute of Geochemistry, Chinese Academy of Sciences, Guangzhou 510640, PR China

[‖]Department of Mechanical and Construction Engineering, Northumbria University, Newcastle upon Tyne, NE1 8ST, UK

[⊥]Department of Architecture and Civil Engineering, University of Bath, Bath, BA2 7AY, UK

E-mail: S.C.Parker@bath.ac.uk; M.Molinari@hud.ac.uk

1

Structures of Mg-Rich Phases

Periclase MgO adopts the face-centred cubic NaCl structure with the $Fm\bar{3}m$ space group[1] in which O^{2-} anions and Mg^{2+} cations are arranged to form face-sharing MgO_6 octahedra.

Magnesite $MgCO_3$ adopts a calcite structure with the the $R\bar{3}c$ space group,[2] comprising alternating layers of Mg^{2+} and CO_3^{2-} ions with each carbonate anion coordinated to three Mg^{2+} cations. $MgCO_3$ is structurally related to MgO, with the a rhombohedral distortion and the carbonate ions occupying the oxygen sites.[2]

Brucite $Mg(OH)_2$ adopts a trignonal $P\bar{3}m1$ structure[3] in which layers of edge-sharing MgO_6 octahedra are stacked along the crystallographic c direction and the H atoms of the hydroxyl HO^- anions project into the interlayer spacing and enable a H-bonding network between layers.

Hydromagnesite $Mg_5(CO_3)_4(OH)_2 \cdot 4\,H_2O$ adopts a monoclinic $P2_1/c$ structure[4,5] comprising a 3D framework of two unique MgO_6 octahedra with Mg^{2+} coordinated either to four carbonate ions, one hydroxyl ion and one water molecule, or to four carbonate and two hydroxyl ions. The hydroxyl groups in the structure are shared between three MgO_6 octahedra and do not participate in H-bonding,[6] while the water molecules are not shared between octahedra and form a 3D H-bonded network.

Nesquehonite $MgCO_3 \cdot 3\,H_2O$ adopts a monoclinic $P2_1/n$ structure[7] composed of 2D chains of corner-sharing MgO_6 octahedra running parallel to the crystallographic b axis. Each octahedron has four equatorial carbonate anions and two axial H_2O molecules, with each CO_3^{2-} ion coordinated to three Mg^{2+} ions. A third uncoordinated H_2O molecule forms a H-bonding network with the carbonate ions and the coordinated water molecules.

Finally, Lansfordite $MgCO_3 \cdot 5\,H_2O$ is a low-temperature phase in the monoclinic $P2_1/a$ space group.[8] The structure comprises two unique MgO_6 octahedra, the first with six H_2O molecules and the second with two carbonate ions and four H_2O molecules, connected by a complex H-bonding network.

Structural Properties

The structure and symmetry of all the Mg-rich phases was retained after minimisation with all the DFT functionals tested. Comparison of the computed structural parameters to experimental measurements shows that the inclusion of van der Waals (vdW) dispersion corrections improves the predicted lattice parameters compared to standard semi-local DFT using the PBE functional. This indicates that the inclusion of a dispersion correction is vital for accurately representing the structures of the phases in the MgO-CO_2-H_2O system, and is therefore required to obtain reliable thermodynamic data.

The overestimation of lattice parameters and unit-cell volumes with PBE is well documented in the literature and is due to the trade off between accurate structures and accurate energetics inherent to GGA functionals.[9] However, it is important to note that experimental measurements are often performed at room temperature, whereas standard DFT optimisations yield "athermal" structures and do not take into account temperature effects. Increasing the temperature generally induces thermal expansion, although some materials do exhibit negative thermal expansion.[10,11] In the usual case of positive thermal expansion, a slight underestimation of the measured lattice parameters in the optimised structures is expected and may indicate good agreement with experiment.

Analysis of the different bonding across the Mg-rich phases leads to some interesting observations. For the Mg-rich phases containing water, *viz.* Lansfordite ($MgCO_3 \cdot 5H_2O$), Nesquehonite ($MgCO_3 \cdot 3H_2O$), Artinite ($Mg_2CO_3(OH)_2 \cdot 3H_2O$) and Hydromagnesite ($Mg_5(CO_3)_4(OH)_2 \cdot 4H_2O$), the DFT functionals including a vdW correction predict a decrease in the cell volume compared to experiment. This is attributed to the vdW corrections providing a better description of the H-bonding in these structures. In keeping with this, all of the functionals predict a similar percentage volume changes with respect to experiment, regardless of whether a vdW correction is applied, for both Magnesite ($MgCO_3$) and Periclase (MgO), which do not contain H_2O.

In contrast, Brucite ($Mg(OH)_2$) shows a much larger variation in volume with the dif-

ferent functionals compared to the other structures. Brucite is a layered structure that is particularly challenging to model, and there is some debate in the literature concerning the nature of the bonding between layers. Work by Bushing et $al.$[12] and a more recent theoretical study by D'Arco et $al.$[13] suggest the interaction between the layers is dominated by vdW forces and that these must therefore be well described in order to obtain the correct interlayer spacing. Kruger et $al.$[14] suggest the interlayer spacing is controlled by H-bonding, which, based on our results for structures containing H_2O, also implies that functionals incorporating vdW corrections should improve upon PBE. Indeed, PBE has the largest overestimation of the interlayer spacing among the functionals tested ($\approx 9\%$), and as a consequence predicts a large expansion of the cell volume.

Finally, $Mg_5(CO_3)_4(OH)_2 \cdot 4\,H_2O$ is another example of a system where the inclusion of vdW corrections greatly improves the structural representation compared to PBE. For this structure optB86b-vdW and optB88-vdW both agree with experimental measurements to within 1%. However, PBE-D3 ($+2\%$) and PBE ($+4\%$) both overestimate the volume, predicting a significant expansion along the b axis. Chaka et $al.$[15] have shown that there are weak vdW interactions along the b axis, which would not be well described in the PBE calculations.

Table S1: Optimised unit-cell parameters of the Mg-rich phases from experiments and DFT calculations: a, b, c (Å), α, β, γ (°) and volume (Å^3). For the lattice constants, the volume and the cell angles not fixed by crystal symmetry, the % differences to experimental values are given in parentheses.

	Expt.	optB86b-vdW	optB88-vdW	PBE-D3	PBE
Lansfordite $MgCO_3 \cdot 5\,H_2O$	Ref.[8]				
a	7.364	7.203 (-2.19%)	7.215 (-2.02%)	7.188 (-2.39%)	7.247 (-1.59%)
b	7.632	7.573 (-0.77%)	7.578 (-0.71%)	7.568 (-0.84%)	7.670 (0.50%)
c	12.488	12.443 (-0.36%)	12.438 (-0.40%)	12.520 (0.26%)	12.650 (1.30%)
$\alpha = \gamma$	90	90	90	90	90
β	101.75	102.44 (0.68%)	102.49 (0.73%)	102.20 (0.44%)	102.22 (0.46%)
Volume	687.14	662.77 (-3.55%)	663.94 (-3.38%)	665.7 (-3.12%)	687.89 (0.11%)
Nequehonite $MgCO_3 \cdot 3\,H_2O$	Ref.[7]				
a	5.365	5.383 (0.34%)	5.382 (0.32%)	5.416 (0.95%)	5.461 (1.79%)
b	12.126	11.904 (-1.83%)	11.919 (-1.71%)	11.874 (-2.08%)	11.912 (-1.76%)
c	7.701	7.561 (-1.82%)	7.562 (-1.80%)	7.600 (-1.31%)	7.755 (0.70%)
$\alpha = \gamma$	90	90	90	90	90
β	90.41	91.51 (1.22%)	91.51 (1.22%)	91.43 (1.13%)	91.35 (1.04%)
Volume	500.98	484.27 (-3.34%)	484.90 (-3.21%)	488.60 (-2.47%)	504.32 (0.67%)
Hydromagnesite	Ref.[4]				
$Mg_5(CO_3)_4(OH)_2 \cdot 4\,H_2O$					
a	10.105	10.041 (-0.63%)	10.043 (-0.61%)	10.103 (-0.02%)	10.161 (0.55%)
b	8.954	9.057 (1.15%)	9.047 (1.04%)	9.109 (1.73%)	9.192 (2.66%)
c	8.378	8.336 (-0.50%)	8.333 (-0.54%)	8.365 (-0.16%)	8.427 (0.58%)
$\alpha = \gamma$	90	90	90	90	90
β	114.44	114.12 (-0.28%)	114.05 (-0.34%)	114.21 (-0.20%)	114.34 (-0.09%)
Volume	690.12	691.94 (0.26%)	691.47 (0.20%)	702.07 (1.73%)	717.16 (3.92%)
Brucite $Mg(OH)_2$	Ref.[3]				
a	6.277	6.310 (0.53%)	6.312 (0.56%)	6.320 (0.69%)	6.374 (1.55%)
b	5.437	5.464 (0.50%)	5.466 (0.53%)	5.470 (0.61%)	5.519 (1.51%)
c	9.007	9.254 (2.74%)	9.31 (3.36%)	9.130 (1.37%)	9.535 (5.86%)
$\alpha = \beta = \gamma$	90	90	90	90	90
Volume	306.27	319.10 (4.19%)	321.19 (4.87%)	315.80 (3.11%)	335.40 (9.51%)
Magnesite $MgCO_3$	Ref.[2]				
$a = b$	4.637	4.661 (0.52%)	4.663 (0.56%)	4.671 (0.73%)	4.693 (1.21%)
c	15.023	14.937 (-0.57%)	14.935 (-0.59%)	15.077 (0.36%)	15.180 (1.05%)
$\alpha = \beta$	90	90	90	90	90
γ	120	120	120	120	120
Volume	279.74	281.04 (0.46%)	281.27 (0.55%)	284.94 (1.86%)	289.58 (3.52%)
Periclase MgO	Ref.[1]				
$a = b = c$	4.217	4.225 (0.19%)	4.227 (0.24%)	4.219 (0.05%)	4.257 (0.95%)
$\alpha = \beta = \gamma$	90	90	90	90	90
Volume	74.99	75.42 (0.57%)	75.54 (0.73%)	75.11 (0.16%)	77.16 (2.89%)

Elastic Constants

We also calculated the bulk modulus B of each structure (Tables S2 and S3), although experimental values for comparison are only available for MgO, $MgCO_3$ and $Mg(OH)_2$.[16–24] There is good agreement between the DFT calculations and experimental measurements for MgO and $MgCO_3$, whereas the bulk modulus of $Mg(OH)_2$ is underestimated due to the overestimated c parameter, which is in turn indicative of a problem with the theoretical description of the interactions between the layers. For all the other structures we can only compare DFT data from different functionals. Despite this, all the methods we tested produce reasonably consistent values for the bulk moduli of each structure, with values within 12 GPa. As the concentration of H_2O per Mg^{2+} ion increases, the bulk modulus decreases, which indicates an inverse relationship between the mechanical compressibility of the structure and the water content. Independent elastic constants for all the phases have also been calculated and are presented in Tables S2 and S3.

Table S2: Calculated bulk moduli B and independent elastic constants (GPa) of Periclase (MgO), Magnesite (MgCo$_3$) and Brucite (Mg(OH)$_2$) obtained from DFT calculations and compared to literature values where available.

	Literature		This Work			
	Expt	Theoretical	optB86b-vdW	optB88-vdW	PBE-D3	PBE
Periclase (MgO)	Ref.[23]	Ref.[24]				
B	163.9	158.0	157.9	159.1	157.3	150.9
C_{11}	299.0	291.0	297	295	299	273
C_{12}	96.4	91.0	88	91	86	90
C_{44}	157.1	139.0	146	148	144	141
Magnesite (MgCO$_3$)	Ref.[19]	Refs.[20–22]				
B	104.6	81.8 - 125	118.8	122.9	114.4	110.6
C_{11}	258.7	223 - 361	261	269	251	242
C_{12}	7.56	56.0 - 93.2	75	78	72	723
C_{13}	5.88	35.9 - 77.7	60	63	57	55
C_{33}	155.5	118 - 187	157	162	153	146
C_{55}	-	42.7	59	60	56	52
Brucite (Mg(OH)$_2$)	Refs.[16,17]	Ref.[18]				
B	50.5 - 55.2	52.3	67.8	67.9	65.4	58.2
C_{11}	154.0 - 159.0	130.6	174	175	171	159
C_{33}	46.36 - 49.7	48.5	80	79	88	54
C_{12}	42.1 - 44.4	70.3	50	50	48	47
C_{13}	7.8 - 11.0	10.0	20	20	19	15
C_{14}	0.2 - 1.3	-	0	0	0	0
C_{44}	21.3 - 22.8	20.4	62	63	61	56

Table S3: Calculated bulk moduli B and independent elastic constants (GPa) of Hydromagnesite ($Mg_5(CO_3)_4(OH)_2 \cdot 4\,H_2O$), Nesquehonite ($MgCO_3 \cdot 3\,H_2O$) and Lansfordite ($MgCO_3 \cdot 5\,H_2O$) obtained from DFT calculations.

	optB86b-vdW	optB88-vdW	PBE-D3	PBE
Hydromagnesite ($Mg_5(CO_3)_4(OH)_2 \cdot 4\,H_2O$)				
B	57.0	57.5	60.6	60.9
C_{11}	109	111	112	110
C_{12}	32	32	36	40
C_{13}	31	31	35	35
C_{15}	1	2	2	0
C_{22}	103	104	105	102
C_{23}	34	35	38	40
C_{25}	2	3	3	1
C_{33}	107	109	110	106
C_{35}	0	2	1	0
C_{44}	32	31	33	34
C_{46}	0	0	0	0
C_{55}	38	37	37	36
C_{66}	39	39	38	37
Nesquehonite ($MgCO_3 \cdot 3\,H_2O$)				
B	49.6	51.2	48.3	43.5
C_{11}	59	60	59	52
C_{12}	19	20	19	17
C_{13}	39	41	37	31
C_{15}	0	0	0	0
C_{22}	96	99	94	92
C_{23}	37	38	36	31
C_{25}	1	1	1	0
C_{33}	101	103	99	89
C_{35}	1	1	1	1
C_{44}	13	13	13	13
C_{46}	0	0	0	0
C_{55}	16	16	16	17
C_{66}	19	19	18	17
Lansfordite ($MgCO_3 \cdot 5\,H_2O$)				
B	45.0	45.8	44.4	40.0
C_{11}	69	69	69	64
C_{12}	39	40	37	31
C_{13}	33	34	32	28
C_{15}	0	0	0	0
C_{22}	58	59	58	54
C_{23}	37	37	36	31
C_{25}	0	0	0	0
C_{33}	62	63	63	61
C_{35}	1	0	1	0
C_{44}	27	27	26	25
C_{46}	0	0	0	0
C_{55}	19	19	20	19
C_{66}	16	16	17	17

Enthalpies of Formation of the Mg-Rich Phases

The enthalpies of formation (ΔH_f^0) were calculated using all four DFT methods and compared to experimental values (Table S4) using Eq. 1, in which elemental species react to produce hydrated and carbonated Mg-rich phases:

$$aM_{(s)} + bH_{2(g)} + cO_{2(g)} + dC_{(s)} \longrightarrow M_a.H_{2b}.O_{2c}.C_{d(s)} \tag{1}$$
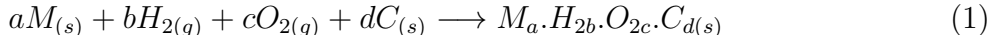
Our theoretical values are calculated without including temperature effects (i.e. at $T = 0$ K) whereas experimental values are at 298 K. It is possible to correct the enthalpies of formation to 0 K, which would result in smaller values, although the changes are typically on the order of 1 %[25] and the correction cannot be applied to all phases due to incomplete experimental data.

Table S4: Enthalpies of formation ΔH_f^0 (kJ/mol) of the Mg-rich phases. The calculated values do not account for temperature effects whereas experimental values are at 298 K.[26] Percentage differences between the calculated and experimental values are shown in parentheses.

	Expt.	optB86b-vdW	optB88-vdW	PBE-D3	PBE
Lansfordite					
$MgCO_3 \cdot 5\,H_2O$	N/A	-2602.02	-2621.44	-2593.19	-2493.99
Nesquehonite					
$MgCO_3 \cdot 3\,H_2O$	-1977.30	-1976.76 (0.03%)	-2000.03 (-1.15%)	-1944.80 (1.64%)	-1882.08 (4.82%)
Hydromagnesite					
$Mg_5(CO_3)_4(OH)_2 \cdot 4\,H_2O$	-6514.90	-6376.57 (2.12%)	-6504.92 (0.15%)	-6151.75 (5.57%)	-5987.67 (8.09%)
Brucite					
$Mg(OH)_2$	-924.50	-897.43 (2.93%)	-922.28 (0.24%)	-874.94 (5.36%)	-838.44 (9.31%)
Magnesite					
$MgCO_3$	-1095.80	-1074.29 (1.96%)	-1100.42 (-0.42%)	-1010.27 (7.81%)	-983.79 (10.22%)
Periclase					
MgO	-601.70	-572.01 (4.93%)	-593.67 (1.33%)	-542.37 (9.86%)	-522.70 (13.13%)

As shown in Table S4, the inclusion of vdW corrections improves the representation of the calculated enthalpies of formation of all the Mg-rich phases compared to PBE, and the optB86b-vdW and optB88-vdW functionals show better performance than PBE-D3.

Comparing the differences between the calculated and experimental ΔH_f^0 per Mg^{2+} ion, for the structures that contain H_2O the DFT techniques that include vdW corrections predict

a decrease (i.e. stabilisation) of approximately 10-20 kJ/mol per H_2O molecule compared to PBE, which improves agreement with experiment. Among the structures that do not contain H_2O, optB86b-vdW and optB88-vdW also show excellent agreement with experiment across a variety of Mg-O bond types (i.e. Mg-OH, Mg-O-CO_2 and Mg-O).
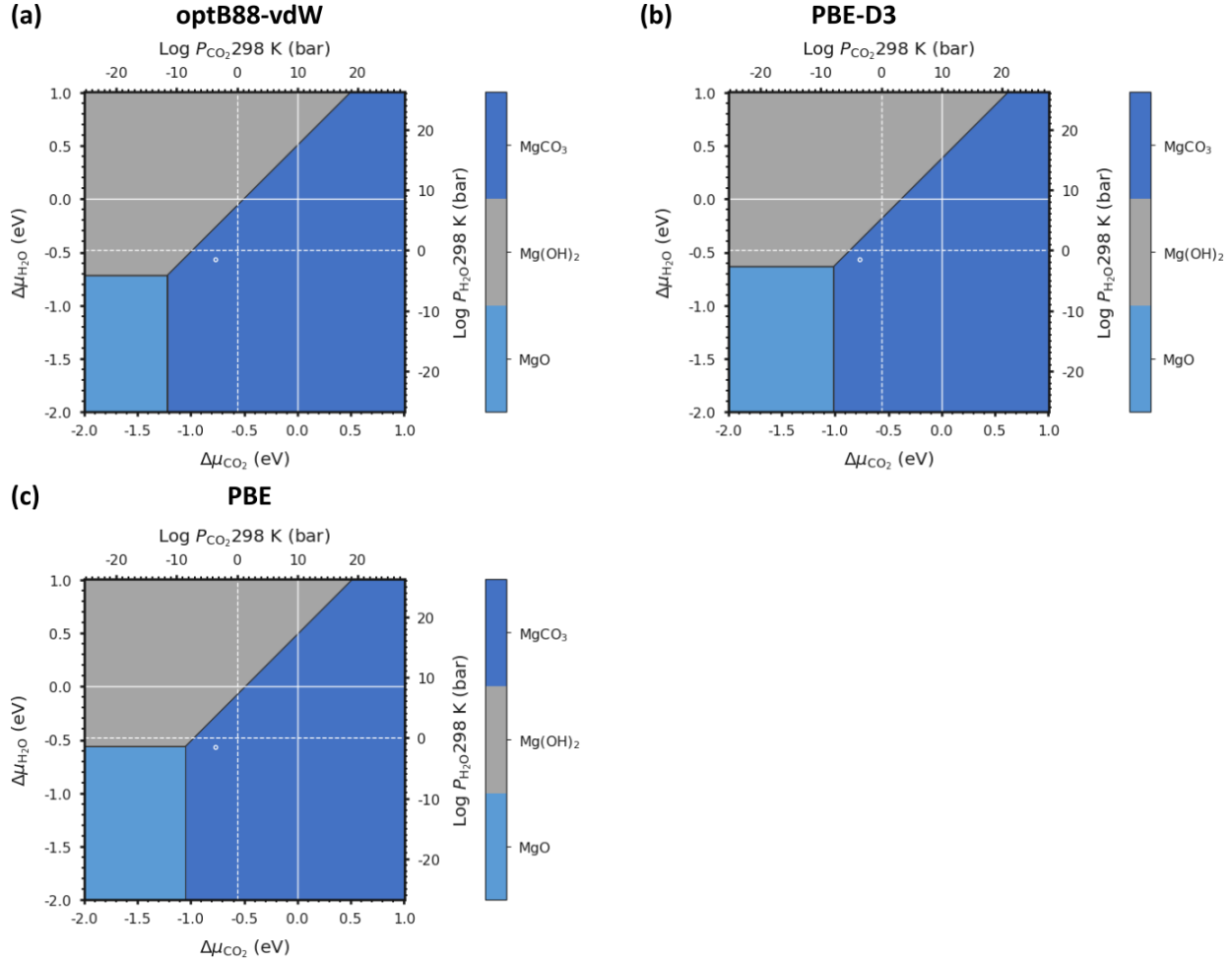
Phase Stability Plots at $T = 0$ K

Figure S1: Phase stability plots of ■ Mg(OH)$_2$, ■ MgO and ■ MgCO$_3$ at $T = 0$ K computed using (a) optB88-vdW, (b) PBE-D3, and (c) PBE. The solid and dashed white lines correspond to 1 bar pressure at 0 K and 298 K respectively.

All the DFT techniques are in good agreement and predict the same Mg-rich phases to be stable under a given set of conditions. However, closer inspection of the phase stability plots reveals small shifts in the location of the phase boundaries. For a fixed $\Delta\mu_{CO_2}$, all the vdW-corrected DFT functionals predict the phase boundaries to occur at a smaller (more negative) $\Delta\mu_{H_2O}$ compared to PBE. It is clearly evident that the inclusion of vdW corrections again provides a better representation of weak and medium-strength bonding. For a given $\Delta\mu_{H_2O}$, PBE-D3 and PBE predict the phase boundaries to occur at a larger (more positive) $\Delta\mu_{CO_2}$

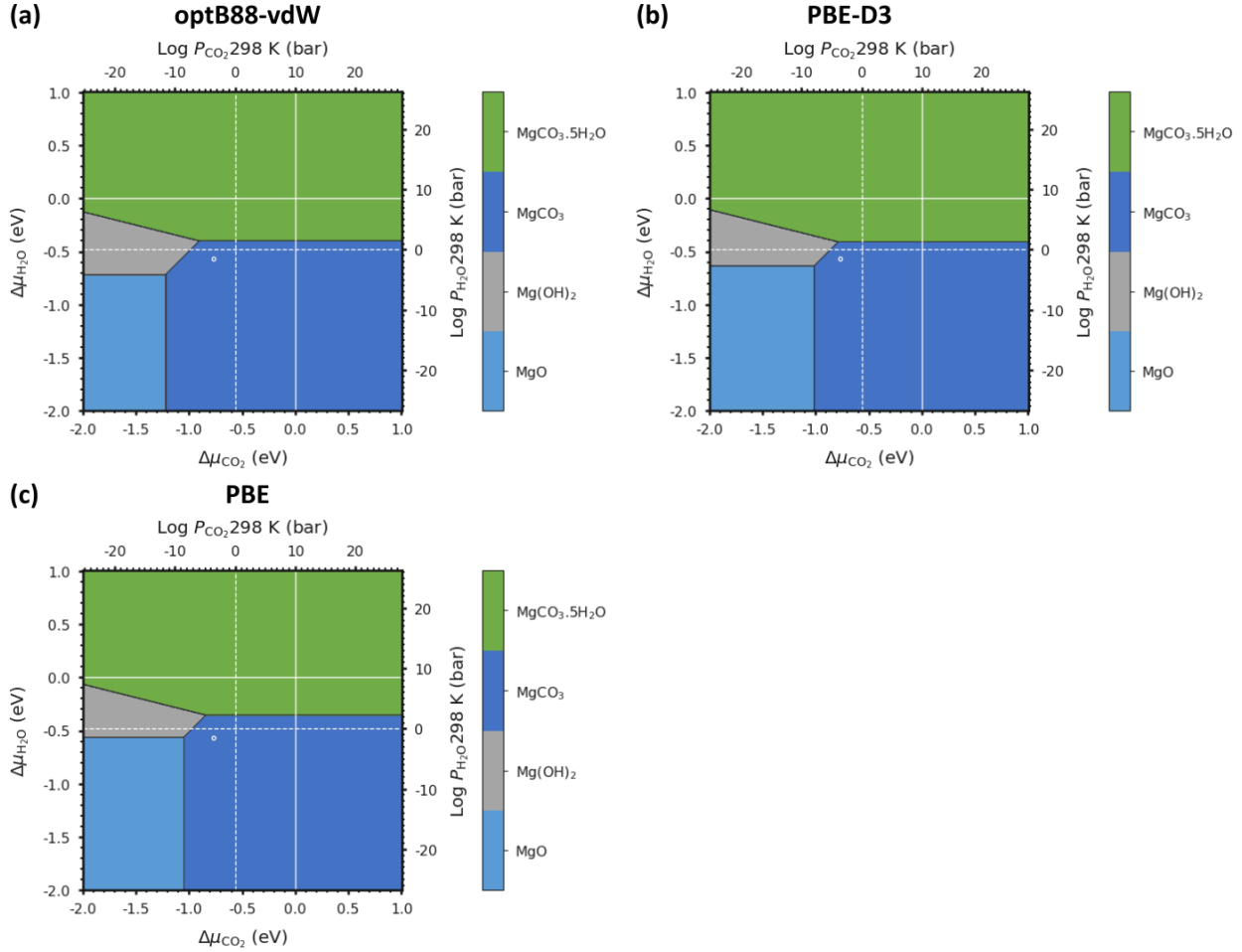Figure S2: Phase stability plots of all Mg-rich phases, *viz.* ■ MgO, ■ MgCO$_3$, ■ Mg(OH)$_2$ and ■ MgCO$_3 \cdot 5\,$H$_2$O, at $T = 0$ K computed using (a) optB88-vdW, (b) PBE-D3 and (c) PBE. The solid and dashed white lines correspond to 1 bar pressure at 0 K and 298 K respectively and the white circle represents atmospheric conditions of 298 K with 400 ppm CO$_2$ and 32 mbar of H$_2$O.

compared to optB86b-vdW and optB88-vdW, which is due to PBE failing to describe the weak vdW interactions accurately. PBE-D3 offers a slight improvement over PBE, but there is still a shift compared to optB86b-vdW and optB88-vdW due to the significant differences between the exchange-correlation treatments.[27]

Predicted Free Energies as a Function of Temperature

Free energies at $p_{\mathrm{CO_2}} = 1$ bar ($\Delta\mu_{\mathrm{CO_2}} = 0$ eV) and $p_{\mathrm{H_2O}} = 1$ bar ($\Delta\mu_{\mathrm{H_2O}} = 0$ eV)
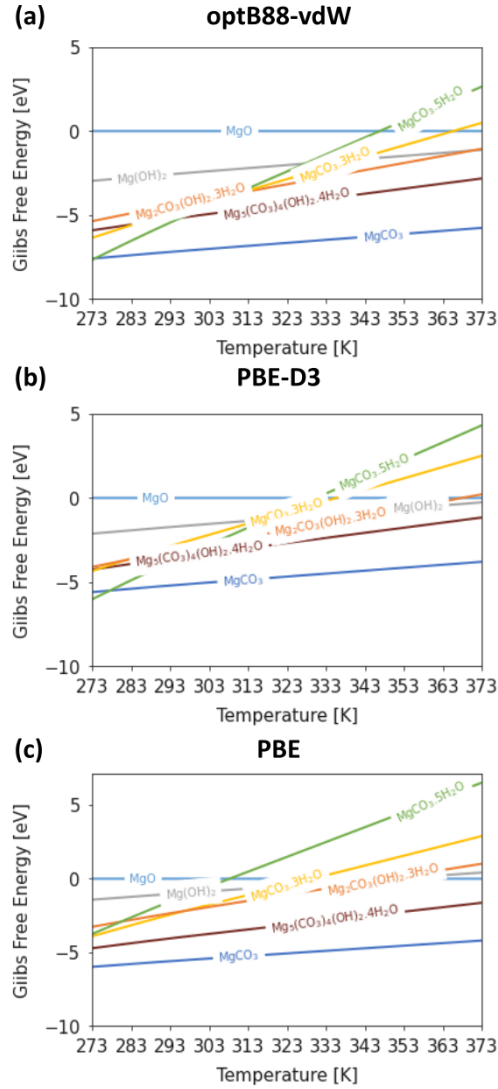
Figure S3: Predicted free energies ΔG_{f}^0 as a function of temperature at $p_{\mathrm{CO_2}} = 1$ bar ($\Delta\mu_{\mathrm{CO_2}} = 0$ eV) and $p_{\mathrm{H_2O}} = 1$ bar ($\Delta\mu_{\mathrm{H_2O}} = 0$ eV) computed using (a) optB88-vdW, (b) PBE-D3 and (c) PBE. Legend: ■ MgO, ■ MgCO$_3$, ■ Mg(OH)$_2$, ■ Mg$_5$(CO$_3$)$_4$(OH)$_2\cdot 4$ H$_2$O, ■ Mg$_2$CO$_3$(OH)$_2\cdot 3$ H$_2$O, ■ MgCO$_3\cdot 3$ H$_2$O and ■ MgCO$_3\cdot 5$ H$_2$O.

Free Energies at Low $p_{CO_2} = 10^{-17}$ bar ($\Delta\mu_{CO_2}$ = -1 eV) and p_{H_2O} = 1 bar ($\Delta\mu_{H_2O}$ = 0 eV)
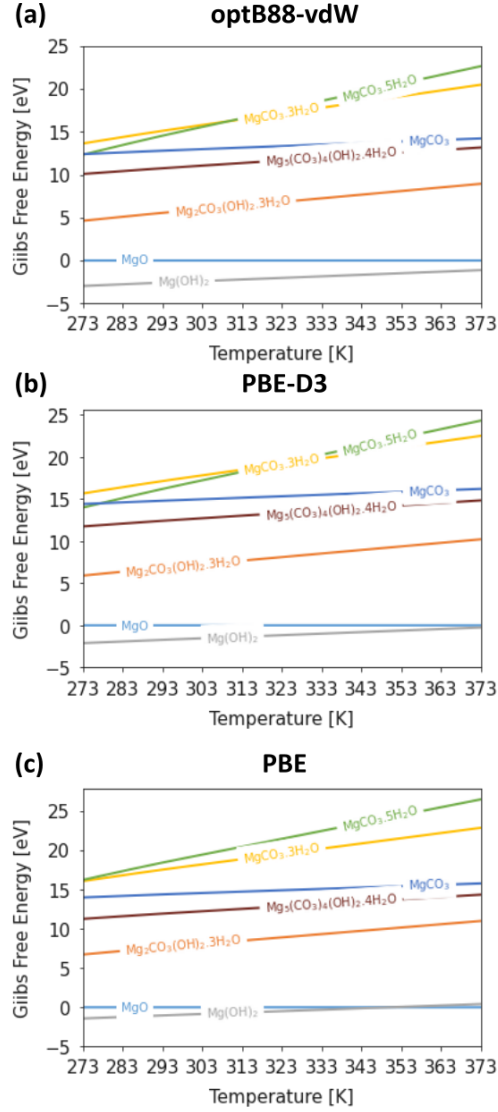

Figure S4: Predicted free energies ΔG_f^0 as a function of temperature at $p_{CO_2} = 10^{-17}$ bar ($\Delta\mu_{CO_2}$ = -1 eV) and p_{H_2O} = 1 bar ($\Delta\mu_{H_2O}$ = 0 eV). Legend: ■ MgO, ■ MgCO$_3$, ■ Mg(OH)$_2$, ■ Mg$_5$(CO$_3$)$_4$(OH)$_2\cdot$4 H$_2$O, ■ Mg$_2$CO$_3$(OH)$_2\cdot$3 H$_2$O, ■ MgCO$_3\cdot$3 H$_2$O and ■ MgCO$_3\cdot$5 H$_2$O.

Free Energies at High $p_{CO_2} = 10^{10}$ bar ($\Delta\mu = 0.6$ eV) and $p_{H_2O} = 1$ bar ($\Delta\mu = 0$ eV)
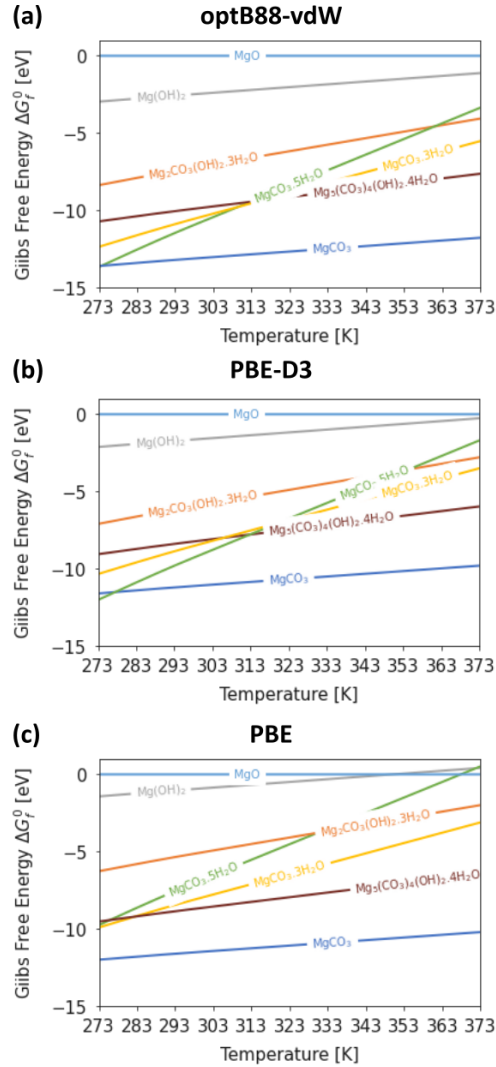

Figure S5: Predicted free energies ΔG_f^0 as a function of temperature at $p_{CO_2} = 10^{10}$ bar ($\Delta\mu_{CO_2} = 0.6$ eV) and $p_{H_2O} = 1$ bar ($\Delta\mu_{H_2O} = 0$ eV). Legend: ■ MgO, ■ MgCO_3, ■ Mg(OH)_2, ■ Mg_5(CO_3)_4(OH)_2·4 H_2O, ■ Mg_2CO_3(OH)_2·3 H_2O, ■ MgCO_3·3 H_2O and ■ MgCO_3·5 H_2O.

Table S5: Predicted phase transition temperatures at $\Delta\mu_{CO_2}$ = -1 eV (p_{CO_2} = 10^{-17} bar) and $\Delta\mu_{H_2O}$ = 0 eV (p_{H_2O} = 1 bar). The symbols > and < indicate that phase transitions are predicted to occur respectively above and below the simulated temperature range.

Phase Transition	optB86b-vdW	optB88-vdW	PBE-D3	PBE
$MgO/Mg(OH)_2$	>	>	>	350
$MgCO_3 \cdot 3\,H_2O/MgCO_3 \cdot 5\,H_2O$	308	310	320	<
$MgCO_3/MgCO_3 \cdot 5\,H_2O$	<	274	277	<

Table S6: Predicted phase transition temperatures at $\Delta\mu_{CO_2}$ = 0 eV (p_{H_2O} = 1 bar) and $\Delta\mu_{CO_2}$ = 0 eV (p_{CO_2} = 1 bar). The symbols > and < indicate that phase transitions are predicted to occur respectively above and below the simulated temperature range.

Phase Transition	optB86b-vdW	optB88-vdW	PBE-D3	PBE
$MgO/Mg_2CO_3(OH)_2 \cdot 3\,H_2O$	>	>	368	349
$MgO/Mg(OH)_2$	>	>	>	350
$MgO/MgCO_3 \cdot 3\,H_2O$	368	366	336	330
$MgO/MgCO_3 \cdot 5\,H_2O$	348	347	330	308
$Mg_2CO_3(OH)_2 \cdot 3\,H_2O/Mg(OH)_2$	>	371	353	348
$Mg_2CO_3(OH)_2 \cdot 3\,H_2O/MgCO_3 \cdot 3\,H_2O$	322	311	282	297
$Mg_2CO_3(OH)_2 \cdot 3\,H_2O/MgCO_3 \cdot 5\,H_2O$	314	310	304	280
$Mg(OH)_2/MgCO_3 \cdot 3\,H_2O$	355	340	316	322
$Mg(OH)_2/MgCO_3 \cdot 5\,H_2O$	336	328	318	299
$MgCO_3 \cdot 3\,H_2O/MgCO_3 \cdot 5\,H_2O$	308	310	320	<
$MgCO_3 \cdot 3\,H_2O/Mg_5(CO_3)_4(OH)_2 \cdot 4\,H_2O$	285	284	275	<
$MgCO_3/MgCO_3 \cdot 5\,H_2O$	<	274	277	<
$MgCO_3 \cdot 5\,H_2O/Mg_5(CO_3)_4(OH)_2 \cdot 4\,H_2O$	296	296	296	<

Table S7: Predicted phase transition temperatures at $\Delta\mu_{CO_2} = 0.6$ eV ($p_{CO_2} = 10^{10}$ bar) and $\Delta\mu_{H_2O} = 0$ eV ($p_{H_2O} = 1$ bar). The symbol $>$ and $<$ indicate that phase transitions are predicted to occur respectivey above and below the simulated temperature range.

Phase Transition	optB86b-vdW	optB88-vdW	PBE-D3	PBE
$MgO/Mg(OH)_2$	$>$	$>$	$>$	350
$MgO/MgCO_3 \cdot 5\,H_2O$	$>$	$>$	$>$	368
$Mg_2CO_3(OH)_2 \cdot 3\,H_2O/MgCO_3 \cdot 5\,H_2O$	365	361	354	330
$MgCO_3 \cdot 3\,H_2O/MgCO_3 \cdot 5\,H_2O$	308	310	320	$<$
$MgCO_3 \cdot 3\,H_2O/Mg_5(CO_3)_4(OH)_2 \cdot 4\,H_2O$	317	316	306	282
$MgCO_3/MgCO_3 \cdot 5\,H_2O$	$<$	274	277	$<$
$Mg(OH)_2/MgCO_3 \cdot 5\,H_2O$	$>$	$>$	$>$	372
$MgCO_3 \cdot 5\,H_2O/Mg_5(CO_3)_4(OH)_2 \cdot 4\,H_2O$	313	313	313	276

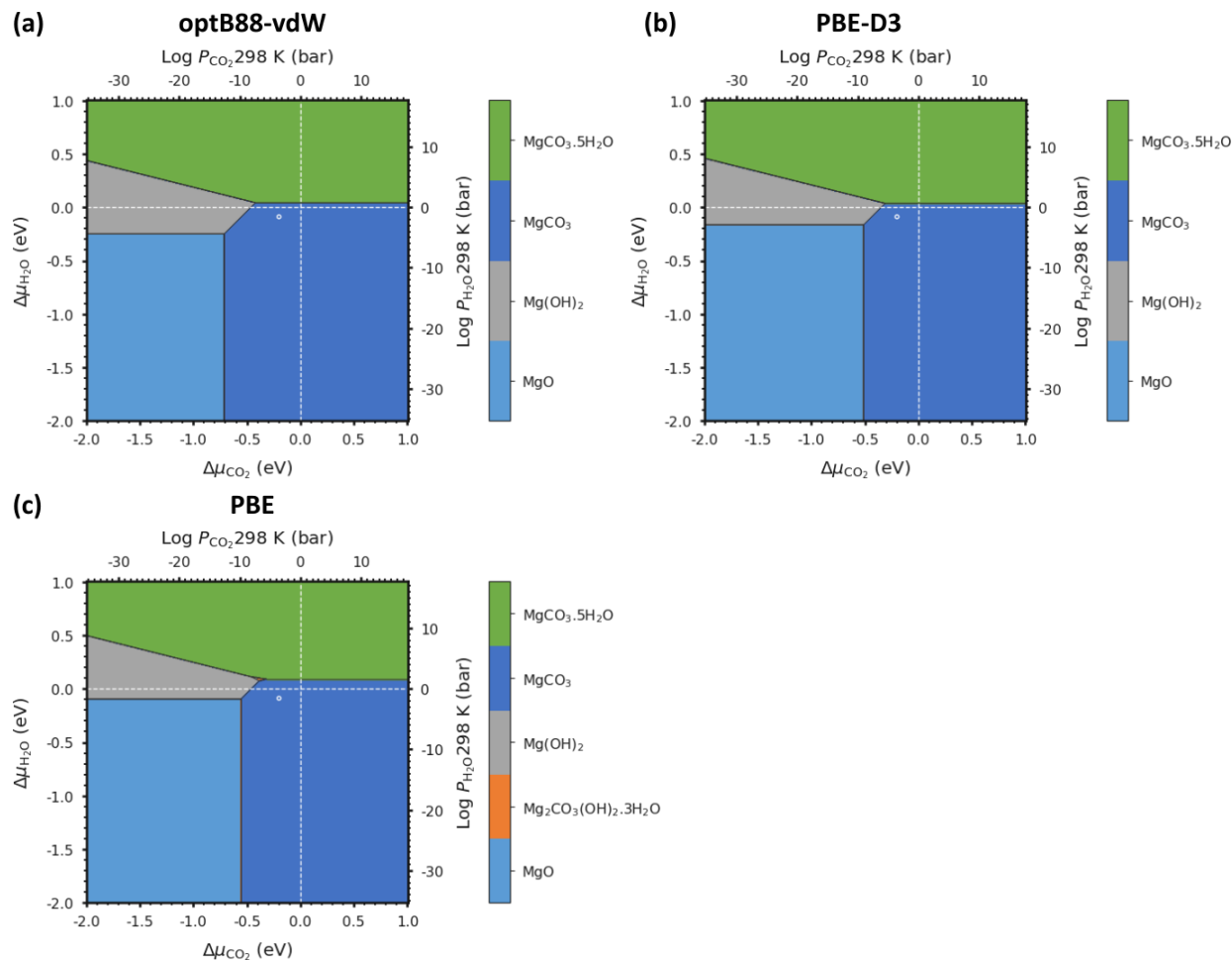# Phase Stability Plots of the Mg-Rich Phases as a Function of $\Delta\mu_{CO_2}$ and $\Delta\mu_{H_2O}$ at 298 K

Figure S6: Predicted phase stability plots of ▮ Periclase (MgO), ▮ Magnesite ($MgCO_3$), ▮ Brucite ($Mg(OH)_2$), ▮ Artinite ($Mg_2CO_3(OH)_2 \cdot 3\,H_2O$) and ▮ Lansfordite ($MgCO_3 \cdot 5\,H_2O$) as a function $\Delta\mu_{CO_2}$ and $\Delta\mu_{H_2O}$ at 298 K obtained using (a) optB88-vdW, (b) PBE-D3 and (c) PBE. On each plot the dashed white line represents $p_{CO_2} = 1$ bar.

Phase Stability Plots of Mg-rich Phases as a Function of $\Delta\mu_{CO_2}$ and Temperature at $\Delta\mu_{H_2O} = 0$ eV ($p_{H_2O} = 1$ bar)
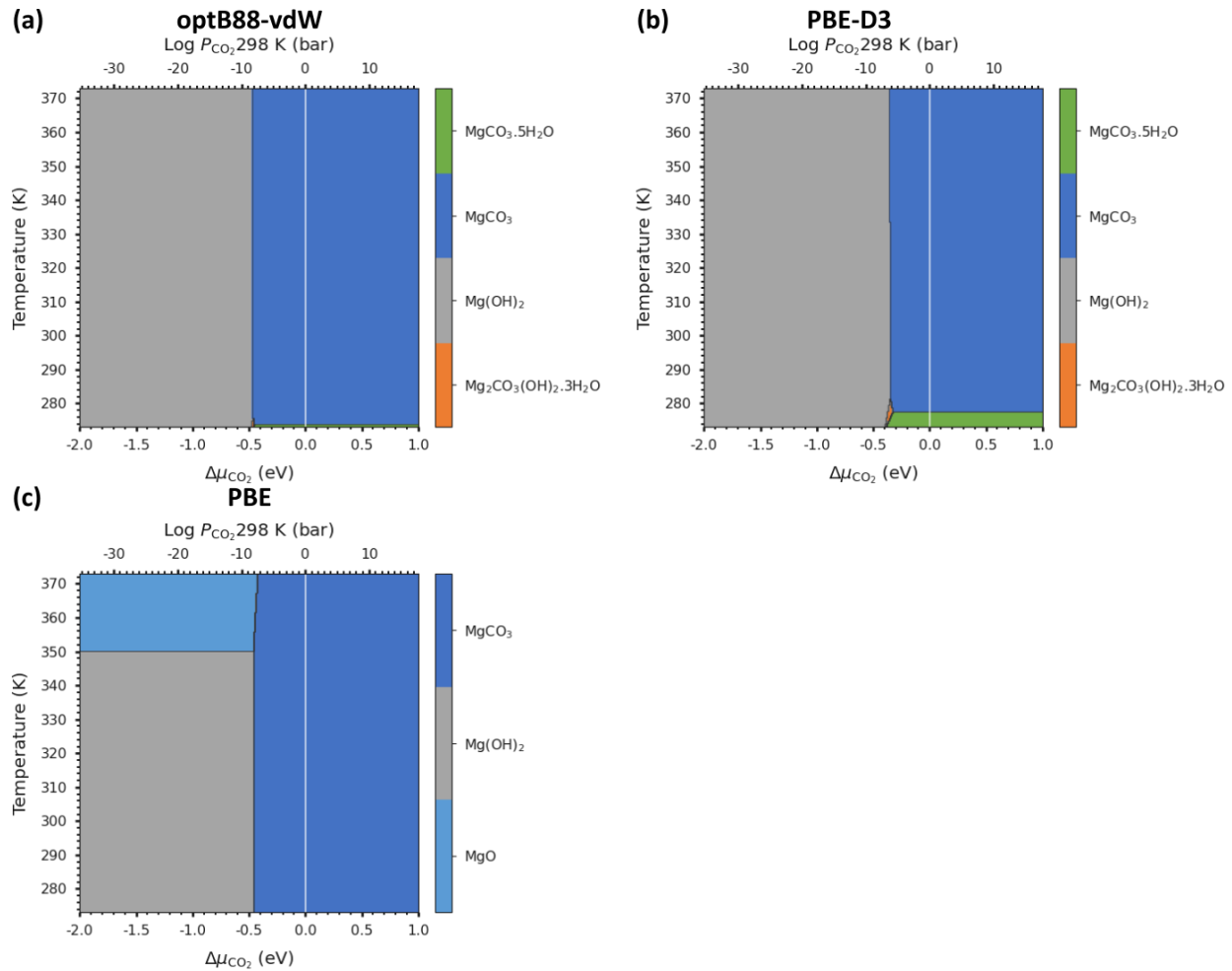
Phase Stability Plots Including All Mg-Rich Phases

Figure S7: Predicted phase stability plots of ■ Periclase (MgO), ■ Magnesite (MgCO$_3$) and ■ Brucite (Mg(OH)$_2$) as a function of $\Delta\mu_{CO_2}$ and temperature at $\Delta\mu_{H_2O} = 0$ eV ($p_{H_2O} = 1$ bar) obtained using (a) optB88-vdW, (b) PBE-D3 and (c) PBE. On each plot the solid white line represents $p_{CO_2} = 1$ bar.

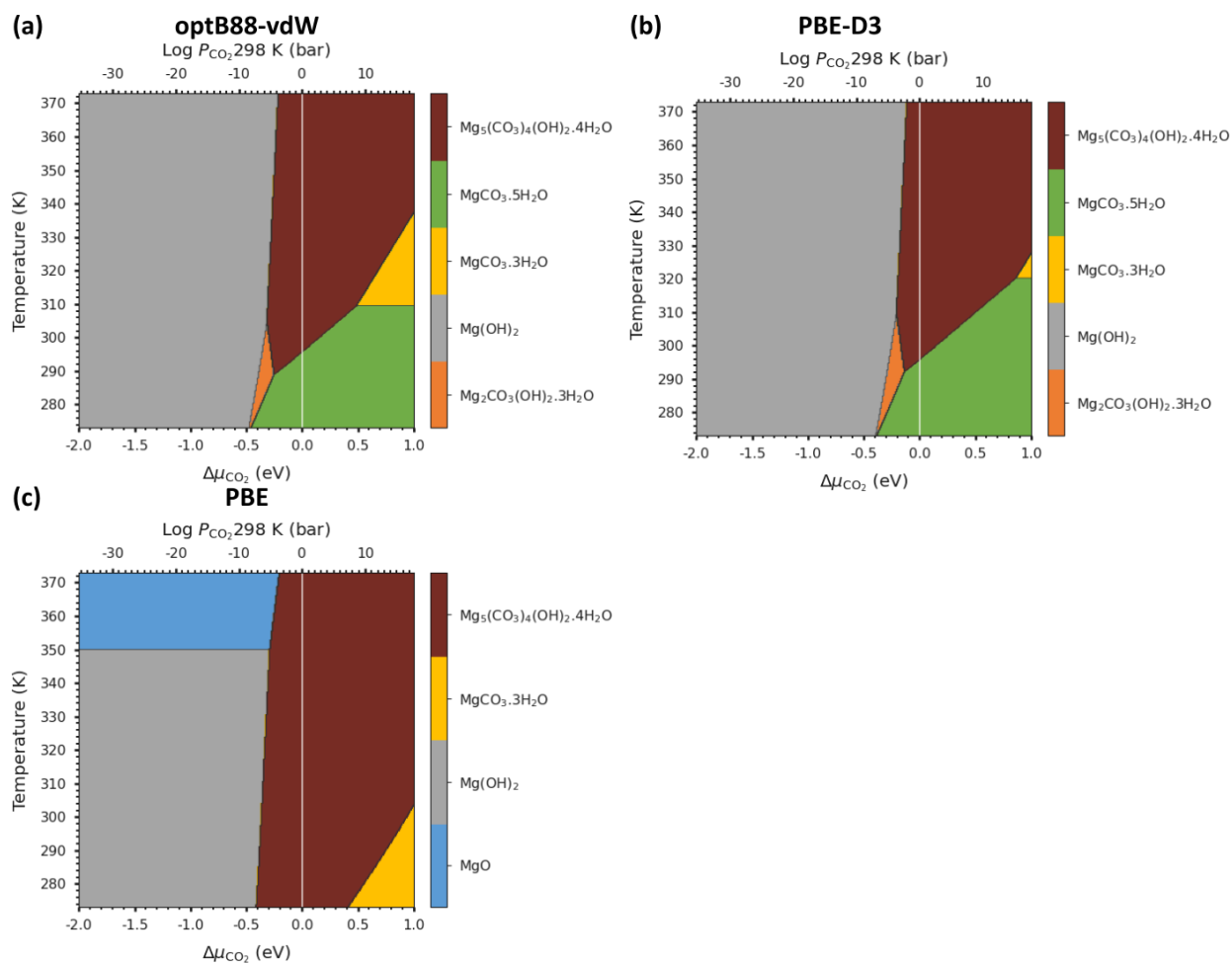# Phase Stability Plots of the Mg-Rich Phases with Magnesite ($MgCO_3$) Inhibited

Figure S8: Predicted phase stability plots of ■ Periclase (MgO), ■ Brucite ($Mg(OH)_2$), ■ Hydromagnesite ($Mg_5(CO_3)_4(OH)_2 \cdot 4\,H_2O$), ■ Artinite ($Mg_2CO_3(OH)_2 \cdot 3\,H_2O$), ■ Nesquehonite ($MgCO_3 \cdot 3\,H_2O$) and ■ Lansfordite ($MgCO_3 \cdot 5\,H_2O$) as a function of $\Delta\mu_{CO_2}$ and temperature at $\Delta\mu_{H_2O} = 0$ eV ($p_{H_2O} = 1$ bar), with Magnesite ($MgCO_3$) inhibited, obtained using (a) optB88-vdW, (b) PBE-D3 and (c) PBE. On each plot the solid white line represents $p_{CO_2} = 1$ bar.

Quasi-Harmonic Free Energy Calculations

Table S8 shows for each of the structures investigated in this work the total number of integrated modes and the number of imaginary modes for each of the volume expansions and compressions used in the quasi-harmonic free energy calculations. For all structures a relatively small percentage of the modes are imaginary, with a maximum of $< 5\%$ in Brucite $(Mg(OH)_2)$. The Artinite structure with a 5% contraction has an imaginary mode at the $q = \Gamma$ wavevector, possibly indicative of an issue during the minimisation, and so this volume was excluded from the QHA calculation.

Table S8: Number of imaginary modes (i-modes) present at each of the volume expansions and compressions used in the quasi-harmonic free-energy calculations relative to the total number of modes.

Volume Change	Total Modes	Integrated Modes	i-modes	% Total	Γ-point i-modes
Artinite $Mg_2CO_3(OH)_2 \cdot 3\,H_2O$					
-5%	6,156,000	6,141,630	14,370	0.23	1
-4%	6,156,000	6,144,839	11,161	0.18	0
-3%	6,156,000	6,154,387	1,613	0.03	0
-2%	6,156,000	6,154,909	1,091	0.02	0
-1%	6,156,000	6,153,497	2,503	0.04	0
0	6,156,000	6,153,345	2,655	0.04	0
1%	6,156,000	6,155,867	133	0.00	0
2%	6,156,000	6,154,303	1,697	0.03	0
3%	6,156,000	6,153,783	2,217	0.04	0
4%	6,156,000	6,151,183	4,817	0.08	0
5%	6,156,000	6,150,381	5,619	0.09	0
Brucite $Mg(OH)_2$					
-5%	120,000	114,653	5,347	4.46	0
-4%	120,000	115,424	4,576	3.81	0
-3%	120,000	116,777	3,223	2.69	0
-2%	120,000	118,238	1,762	1.47	0
-1%	120,000	119,100	900	0.75	0

Table S8: Number of imaginary modes (i-modes) present at each of the volume expansions and compressions used in the quasi-harmonic free-energy calculations relative to the total number of modes.

Volume Change	Total Modes	Integrated Modes	i-modes	% Total	Γ-point i-modes
0	120,000	119,441	559	0.47	0
1%	120,000	119,728	272	0.23	0
2%	120,000	119,906	94	0.08	0
3%	120,000	119,737	263	0.22	0
4%	120,000	119,888	112	0.09	0
5%	120,000	119,692	308	0.26	0
Hydromagnesite $Mg_5(CO_3)_4(OH)_2 \cdot 4\,H_2O$					
-5%	5,994,000	5,993,997	0	0.00	0
-4%	5,994,000	5,993,997	0	0.00	0
-3%	5,994,000	5,993,997	0	0.00	0
-2%	5,994,000	5,993,997	0	0.00	0
-1%	5,994,000	5,993,997	0	0.00	0
0	5,994,000	5,993,467	533	0.01	0
1%	5,994,000	5,993,815	185	0.00	0
2%	5,994,000	5,993,921	79	0.00	0
3%	5,994,000	5,993,969	31	0.00	0
4%	5,994,000	5,993,905	95	0.00	0
5%	5,994,000	5,993,783	217	0.00	0
Lansfordite $MgCO_3 \cdot 5\,H_2O$					
-5%	6,480,000	6,476,085	3,915	0.06	0
-4%	6,480,000	6,476,313	3,687	0.06	0
-3%	6,480,000	6,475,363	4,637	0.07	0
-2%	6,480,000	6,475,563	4,437	0.07	0
-1%	6,480,000	6,476,735	3,265	0.05	0
0	6,480,000	6,478,401	1,599	0.02	0
1%	6,480,000	6,478,743	1,257	0.02	0
2%	6,480,000	6,479,195	805	0.01	0
3%	6,480,000	6,479,101	899	0.01	0
4%	6,480,000	6,479,373	627	0.01	0
5%	6,480,000	6,477,827	2,173	0.03	0

Table S8: Number of imaginary modes (i-modes) present at each of the volume expansions and compressions used in the quasi-harmonic free-energy calculations relative to the total number of modes.

Volume Change	Total Modes	Integrated Modes	i-modes	% Total	Γ-point i-modes
Magnesite $MgCO_3$					
-5%	9,953,280	9,950,591	2,689	0.03	0
-4%	9,953,280	9,951,073	2,207	0.02	0
-3%	9,953,280	9,951,927	1,353	0.01	0
-2%	9,953,280	9,953,277	0	0.00	0
-1%	9,953,280	9,950,349	2,931	0.03	0
0	9,953,280	9,953,277	0	0.00	0
1%	9,953,280	9,951,383	1,897	0.02	0
2%	9,953,280	9,952,365	915	0.01	0
3%	9,953,280	9,950,231	3,049	0.03	0
4%	9,953,280	9,951,791	1,489	0.01	0
5%	9,953,280	9,953,277	0	0.00	0
Periclase MgO					
-5%	1,119,744	1,119,743	0	0.00	0
-4%	1,119,744	1,119,742	0	0.00	0
-3%	1,119,744	1,119,741	0	0.00	0
-2%	1,119,744	1,119,743	0	0.00	0
-1%	1,119,744	1,119,743	0	0.00	0
0	1,119,744	1,119,741	0	0.00	0
1%	1,119,744	1,119,742	0	0.00	0
2%	1,119,744	1,119,742	0	0.00	0
3%	1,119,744	1,119,742	0	0.00	0
4%	1,119,744	1,119,742	0	0.00	0
5%	1,119,744	1,119,742	0	0.00	0
Nesquehonite $MgCO_3 \cdot 3\,H_2O$					
-5%	4,536,000	4,529,105	6,895	0.15	0
-4%	4,536,000	4,532,253	3,747	0.08	0
-3%	4,536,000	4,532,347	3,653	0.08	0
-2%	4,536,000	4,532,995	3,005	0.07	0
-1%	4,536,000	4,533,865	2,135	0.05	0

Table S8: Number of imaginary modes (i-modes) present at each of the volume expansions and compressions used in the quasi-harmonic free-energy calculations relative to the total number of modes.

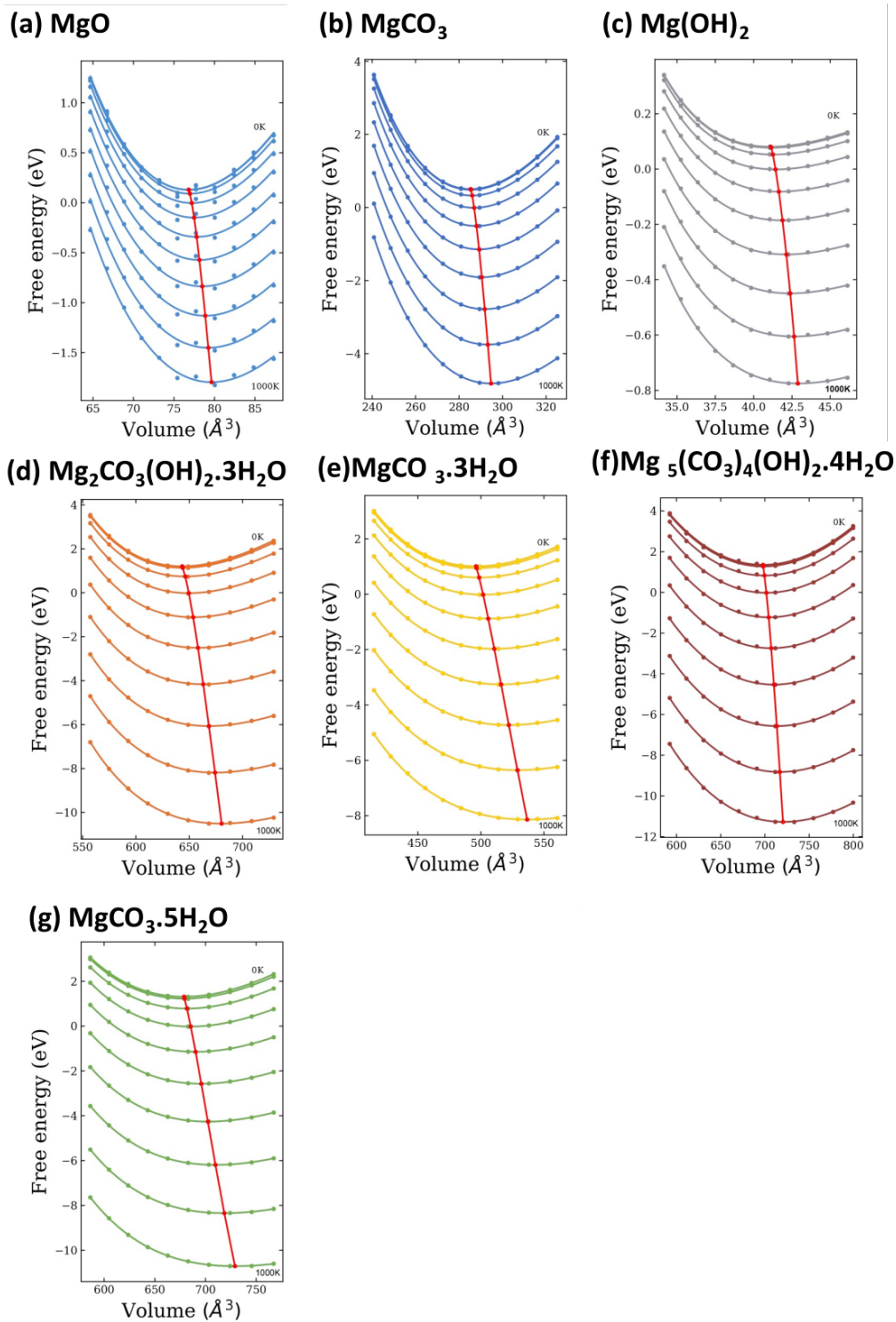| Volume Change	Total Modes	Integrated Modes	i-modes	% Total	Γ-point i-modes
0	4,536,000	4,533,525	2,475	0.05	0
1%	4,536,000	4,534,165	1,835	0.04	0
2%	4,536,000	4,534,581	1,419	0.03	0
3%	4,536,000	4,534,503	1,497	0.03	0
4%	4,536,000	4,534,133	1,867	0.04	0
5%	4,536,000	4,532,389	3,611	0.08	0

Figure S9: Helmholtz free energy as a function of volume equation of state (EoS) curves for each phase simulated for temperatures from 0-1000 K in 100 K steps. On each plot the red line marks the equilibrium volume as a function of temperature, determined as the minimum on each of the EoS curves.

References

(1) Sasaki, S.; Fujino, K.; Takeuchi, Y. X-Ray Determination of Electron-Density Distributions in Oxides, MgO, MnO, CoO, and NiO, and Atomic Scattering Factors of their Constituent Atoms. *Proc. Jpn. Acad., Ser. B* **1979**, *55*, 43–48.

(2) K. D. Oh, S. I., H. Morikawa; Aoki, H. The Crystal Structure of Magnesite. *Am. Mineral.* **1973**, *58*, 480–494.

(3) Catti, M.; Ferraris, G.; Hull, S.; Pavese, A. Static Compression and H Disorder in Brucite, $Mg(OH)_2$, to 11 GPa: a Powder Neutron Diffraction Study. *Phys. Chem. Miner.* **1995**, *22*, 200–206.

(4) Akao, M.; Iwai, S. The Hydrogen Bonding of Hydromagnesite. *Acta Crystallogr., Sect. B* **1977**, *33*, 1273–1275.

(5) Akao, M.; Marumo, F.; Iwai, S. The Crystal Structure of Hydromagnesite. *Acta Crystallogr., Sect. B* **1974**, *30*, 2670–2672.

(6) Hollingbery, L. A.; Hull, T. R. The Thermal Decomposition of Huntite and Hydromagnesite-A review. *Thermochim Acta* **2010**, *509*, 1–11.

(7) Giester, G.; Lengauer, C. L.; Rieck, B. The Crystal Structure of Nesquehonite, $MgCO_3.3H_2O$, from Lavrion, Greece. *Mineral. Petrol.* **2000**, *70*, 153–163.

(8) Hill, R. J.; Canterford, J. H.; Moyle, F. J. New Data for Lansfordite. *Mineral. Mag.* **1982**, *46*, 453–457.

(9) van de Walle, A.; Ceder, G. Correcting Overbinding in Local-Density-Approximation Calculations. *Phys. Rev. B* **1999**, *59*, 14992–15001.

(10) Parker, S. C.; Price, G. D. Computer Modelling of Phase Transitions in Minerals. *Adv. Solid-State Chem.* **1989**, *1*, 295–327.

(11) Tschaufeser, P.; Parker, S. C. Thermal Expansion Behavior of Zeolites and AlPO4s. *J. Phys. Chem.* **1995**, *99*, 10609–10615.

(12) Busing, W. R.; Levy, H. A. Neutron Diffraction Study of Calcium Hydroxide. *J. Phys. Chem.* **1957**, *26*, 563–568.

(13) D'Arco, P.; Causà, M.; Roetti, C.; Silvi, B. Periodic Hartree-Fock Study of a Weakly Bonded Layer Structure: Brucite $Mg(OH)_2$. *Phys. Rev. B* **1993**, *47*, 3522–3529.

(14) Kruger, M.; Williams, Q.; Jeanloz, R. Vibrational-Spectra of $Mg(OH)_2$ and $Ca(OH)_2$ Under Pressure. *J. Chem. Phys.* **1989**, *91*, 5910–5915.

(15) Chaka, A. M.; Felmy, A. R. Ab Initio Thermodynamic Model for Magnesium Carbonates and Hydrates. *J. Phys. Chem. A* **2014**, *118*, 7469–7488.

(16) Jiang, F.; Speziale, S.; Duffy, T. S. Single-Crystal Elasticity of Brucite, $Mg(OH)_2$, to 15 GPa by Brillouin Scattering. *Am. Mineral.* **2006**, *91*, 1893–1900.

(17) Xia, X.; Weidner, D. J.; Zhao, H. Equation of State of Brucite: Single-Crystal Brillouin Spectroscopy Study and Polycrystalline Pressure-Volume-Temperature Measurement. *Am. Mineral.* **1998**, *83*, 68–74.

(18) Jochym, P. T.; Oleś, A. M.; Parlinski, K.; Łażewski, J.; Piekarz, P.; Sternik, M. Structure and Elastic Properties of $Mg(OH)_2$ from Density Functional Theory. *J. Phys.: Condens. Matter* **2010**, *22*, 445403.

(19) Humbert, M. M. P.; Plicque, F. Propriétés Elastiques de Carbonates Rhomboédriques Monocristallins : Calcite, Magnésite, Dolomie. *C. R. Seances Acad. Sci., Vie Acad.* **1972**, *275*, 391–394.

(20) Brik, M. G. First-Principles Calculations of Structural, Electronic, Optical and Elastic Properties of Magnesite $MgCO_3$ and Calcite $CaCO_3$. *Phys. B* **2011**, *406*, 1004 – 1012.

(21) Catti, M.; Pavese, A.; Dovesi, R.; Saunders, V. R. Static Lattice and Electron Properties of MgCO$_3$ (Magnesite) Calculated by Ab Initio Periodic Hartree-Fock Methods. *Phys. Rev. B* **1993**, *47*, 9189–9198.

(22) Liu, Z. J.; Sun, X. W.; Song, T.; Guo, Y.; Zhang, C. R.; Zhang, Z. R. Atomistic Simulation of the Structural and Elastic Properties of Magnesite. *Bull. Mater. Sci.* **2016**, *39*, 1319–1325.

(23) Isaak, D. G.; Anderson, O. L.; Goto, T. Measured Elastic Moduli of Single-Crystal MgO up to 1800 K. *Phys. Chem. Miner.* **1989**, *16*, 704–713.

(24) Karki, B. B.; Stixrude, L.; Clark, S. J.; Warren, M. C.; Ackland, G. J.; Crain, J. Structure and Elasticity of MgO at High Pressure. *Am. Mineral.* **1997**, *82*, 51–60.

(25) Chase, M. W.; National Institute of Standards; Technology (U.S.), *NIST-JANAF Thermochemical Tables*, 4th ed.; J. Phys. Chem. Ref. Data, Monogr.; 1998.

(26) Weast, R. C. *CRC Handbook of Chemistry & Physics 61st Edition*; CRC Press Inc., 1980.

(27) Klimeš, J.; Michaelides, A. Perspective: Advances and Challenges in Treating van der Waals Dispersion Forces in Density Functional Theory. *J. Chem. Phys.* **2012**, *137*, 120901.